A computerized method of contact pressure and load distribution for crossed beveloid gears

A computerized method of contact pressure and load distribution for crossed beveloid gears

Bing Cao [a,b,c], Fortunato Alessandro [c], Guolong Li [a,b,*], Yijie Tao [a,b], Quanfu Ran [a,b]

[a] State Key Laboratory of Mechanical Transmissions, Chongqing University, Chongqing 400044, China
[b] College of Mechanical and Vehicle Engineering, Chongqing University, Chongqing 400044, China
[c] Department of Industrial Engineering (DIN), Alma Mater Studiorum-University of Bologna, Viale Risorgimento 2, 40136, Bologna, Italy

A B S T R A C T

Exact contact pressure and load distribution are key evaluation indices for beveloid gear design. A numerical calculation approach of contact pressure and load distribution for crossed beveloid gears is proposed, as opposed to the traditional method based on a finite element modeling software package. To acquire the flexibility properties of beveloid gear tooth surfaces, an accurate finite element (FE) model about a beveloid gear tooth with root fillets is first built. A solution model for crossed beveloid gears is developed using the influence coefficients technique. An enhanced solving approach is presented to improve the robustness of the solving model by addressing the limitation of the influence coefficients method. In addition, a unique contact pressure is presented. The numerical example proposed can be used to test the proposed methodology.

Keywords:
Beveloid gear
Crossed axis
Contact pressure
Load distribution
Influence coefficients method

1. Introduction

With the increasing demand of high strength for gear transmission systems, contact pressure and load distribution have been key evaluation indexes to design and optimize gear pairs' macro and micro parameters [1–3]. Collaborative tooth surface optimization considering both geometric and physical performances is always an active point in tooth flank design for gears [4–6]. At present, loaded tooth contact analysis based on commercial software packages such ABAQUS and ANSYS is a main solution to obtain exact contact pressure and load distribution [7,8]. As introduced by Ding [9], it has the following deficiencies:

(i) High computational cost. Commercial software tools for load teeth contact analysis are based on accurate finite element modeling, as well as generating, assembling, and meshing 3D solid models. An analysis usually takes a few days.

(ii) Poor flexibility. The workflow of the method precludes it from having high flexibility. It's difficult to change and process the results immediately. In terms of modification optimization, all 3D models matching to each set of gear parameters must be developed, assembled, and meshed. Furthermore, we can only adjust the model if the outcomes are problematic, but the provided model is normally fixed.

As a result, using this method to undertake a continuous optimization for gear pairs is difficult. Some novel ways have recently been reported. Simon developed hypoid and helical gear estimation methods by using regression analysis findings from calculated deflection and displacement under load based on FE models [10–13]. Fang calculated the load distribution of crossed helical gears using finite element method(FEM) to calculate flexibility [14]. Hou introduced a contact analysis algorithm based on modified VFIFE

method and verified the feasibility of the algorithm by comparing the results with the ABAQUS simulation results [15]. Pedrero proposed a load distribution model based on the minimum elastic potential criteria for the calculation of tooth bending strength and surface durability [16]. Using the model introduced by Pedrero, Sa´nchez further developed a calculation method of contact stress along the line of action [17]. Rameshkumar developed FEM for determining the load distribution of high-contact-ratio spur gears [18, 19]. Based on the influence coefficient method, Tsai developed a method for load contact analysis of high-contact-ratio spur gear considering flank modification [20]. Applying the Hertz contact theory, Volkov proposed an algorithm for contact stress analysis of gears, that characterized with realizing the calculation of contact stress for multi-pair contact [21]. Gosselin proposed a curve-fitting method to determine the tooth elastic contact deformation [22]. Using semi-analytical, Rayleigh-Ritz based shell model of the teeth to calculate the tooth compliance, Kahraman proposed a load distribution model for hypoid gears using ease-off topography [23]. Based on the double-curved shell theory and Rayleigh-Ritz method, Ding [9] developed a numerical load contact analysis method for spiral bevel and hypoid gears.

In terms of beveloid gears, few researches has been reported. Zhu analyzed the effect of rack-cutter parabolic modification on load contact characteristics, where the analysis was based on ABAQUS software [2]. Using the influence coefficient method, Tsai introduced a method for analysis of skew conical gear drives in approximate line contact, where influence coefficient calculation was based on the Boussinesq half-space force-displacement relations to calculate the contact deformation and the bending deformation coefficient's calculation is based on the result of FEM for involute cylindrical gears [24,25]. Considering the asymmetric the left and right tooth surfaces of beveloid gears, Song established a mesh stiffness calculation model of paralleled helical beveloid gear pair based on potential energy theory [26]. They further analyzed the effect of pitting defect on the mesh stiffness for straight beveloid gear [27].

Above references significantly improve the efficiency and accuracy of contact pressure and load distribution, but they focused on spur gears or spiral bevel and hypoid gears. As an analytical tooth compliance determination method, Rayleigh-Ritz method only is valid for gears with constant height along tooth width direction and either constant or linearly varying thickness along their profile [28,29]. Beveloid gears are not the case. It is worth noting that because the beveloid gears under crossed axes can achieve point contact, approximate line contact and line contact, the contact may be the non-Hertzian contact. The influence coefficient method can be used to calculate the contact pressure analysis for crossed beveloid gears with approximate line contact [25]. Because of the asymmetric the left and right tooth surfaces of helical beveloid gears, the calculation method applied by Tsai cannot be applied to helical beveloid gears [24,30]. Therefore, the references about beveloid gears focused on the straight beveloid gears.

It is worth noting that there are two defects for the influence coefficient method. The first is the estimation value of contact stress increases, and the result fluctuation amplitude obviously increases with the dimension of contact area element decreasing, which cause negative influence on the accurate estimation of pressure value. The second is the dimension of contact area element needs to be infinitesimal to achieve the estimation of the exact contact stress. However, no research was reported to determine the dimension of contact area elements. Therefore, the above two defects need to be considered in using the influence coefficient method.

In the present study, the influence coefficient method is applied to calculate the load distribution of crossed beveloid gears. Firstly, a finite element model for a beveloid gear tooth with root fillet is developed. By applying three directions' unit force and extracting the displacement including deformations, the flexibility characteristics of nodes at tooth surfaces can be obtained. Based on the influence coefficient method and deformation compatibility within contact area, a solving model is established. To improve the robustness of the calculation model, an enhanced solving method is proposed. Here, the initial contact area is estimated more accurately, and preconditioning method is applied to decrease the condition number. Considering the defects of the influence coefficient method, a novel estimation method is proposed to achieve accurate estimation of contact pressure. By a numerical example, the feasibility of the method is validated.

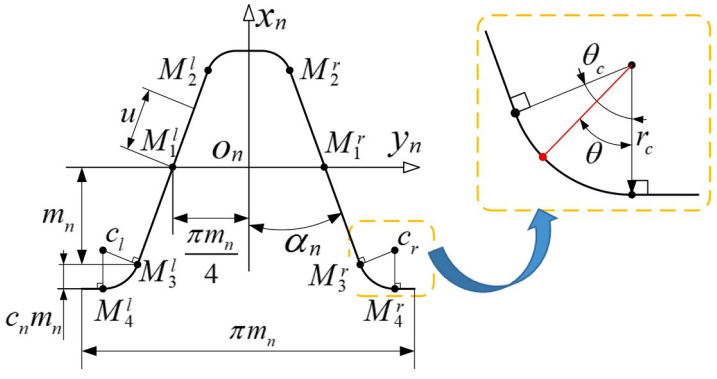

Fig. 1. Normal sections of rack-cutter.

2. Flexibility characteristics of beveloid gears

2.1. Mathematical model of beveloid gear with root fillet

The force-displacement relation between the contact points within a contact region is an essential factor in the solving model based on the influence coefficient method. Contact deformation, tooth bending deformation and shear deformation occur when a force is applied to any position on the tooth surface. The accurate tooth model is the premise of calculating all deformations.

According to the generation concept introduced by Merrit [31], beveloid gears are enveloped by a rack-cutter. Compared with conventional involute gear's generating, it is characterized by that the generating rack-cutter's pitch plane intersects the axis of enveloped beveloid gears, which forms an angle, i.e. the beveloid gear cone angle.

Fig. 1 shows the normal sections with fillet of the rack cutter. The straight line $M_3^l M_2^l$ and $M_3^r M_2^r$ generate the involute tooth profiles. The fillet curve $M_4^l M_3^l$ and $M_4^r M_3^r$ generate the root fillet of beveloid gears. The plane $y_n o_n z_n$ is the pitch plane of the rack-cutter. The length of $o_n M_1^l$ is the same as the one of $o_n M_1^r$. In the coordinate system s_n, the geometry of $M_3^l M_2^l$ and $M_3^r M_2^r$ can be expressed as:

$$\boldsymbol{R}_n^{pj}(u) = \begin{bmatrix} u\cos\alpha_n \\ \pm\dfrac{\pi m_n}{4} + u\sin\alpha_n \\ 0 \end{bmatrix} (j = l, r) \tag{1}$$

where the subscript represents the coordinate system; the upper of $\pm$ or $+$ is for the right profile. u is the length between any point and M_1^l or M_1^r; α_n and m_n are the normal pressure angle and the normal module of the rack-cutter.

The fillet curves denoted by $M_4^l M_3^l$ and $M_4^r M_3^r$ can be expressed in the coordinate system s_n as:

$$\boldsymbol{R}_n^{cj} = \begin{bmatrix} -m_n + r_c(\cos\theta_c - \cos\theta) \\ \pm\dfrac{\pi m_n}{4} \pm m_n\tan\alpha_n + r_c(\pm\sin\theta_c + \sin\theta) \\ 0 \end{bmatrix} (j = l, r) \tag{2}$$

where r_c is the radius of the fillet curves and determined by a designer. θ_c is the included angle of the fillet curves, which can be represented as:

$$\theta_c = \frac{\pi}{2} - \alpha_n \tag{3}$$

Based on the generating concept, the envelope process of a rack-cutter generating beveloid gears is described in Fig. 2. Herein, five coordinate systems s_n, s_p, s_c, s_g and s_f are introduced. The plane $x_p o_p y_p$ is parallel with the end section of the rack-cutter and forms the included angle β with the plane $x_n o_n y_n$. The plane $y_c o_c z_c$ is tangent to the beveloid gear's pitch cylinder. It forms the cone angle δ of the beveloid gear with the plane $y_n o_n z_n$. The coordinate system s_n, s_p and s_c are rigidly connected to the rack-cutter. The coordinate system s_g is rigidly connected to the generated beveloid gear. The coordinate system s_f is a reference coordinate system.

For any plane P parallel with the plane $x_n o_n y_n$ and distance l to it, the section at the plane is the same as the one in the plane $x_n o_n y_n$. Therefore, the geometry of the rack-cutter in the coordinate system s_n can be represented as:

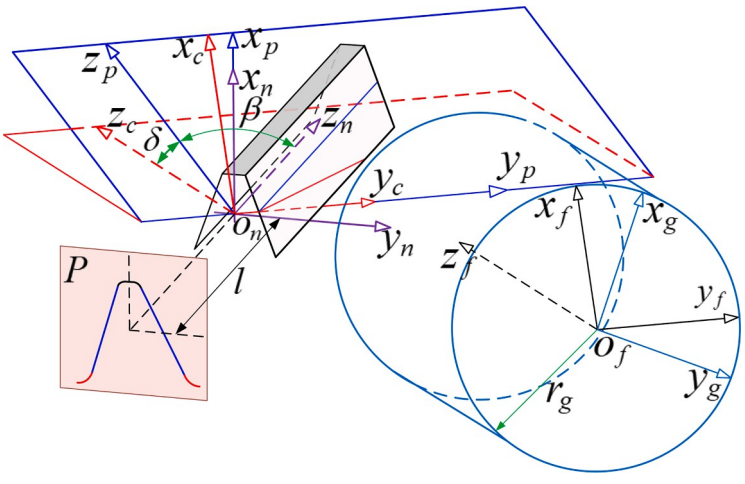

Fig. 2. Generating mechanism of beveloid gears.

$$\boldsymbol{R}_n^{pf-j}(u,l)=\begin{bmatrix} u\cos\alpha_n \\ \pm\dfrac{\pi m_n}{4}+u\sin\alpha_n \\ l \end{bmatrix}(j=l,r) \tag{4}$$

$$R_n^{cf-j}(\theta,l)=\begin{bmatrix} -m_n+r_c(\cos\theta_c-\cos\theta) \\ \pm\dfrac{\pi m_n}{4}\pm m_n\tan\alpha_n+r_c(\pm\sin\theta_c+\sin\theta) \\ l \end{bmatrix}(j=l,r) \tag{5}$$

Based on the differential geometry theory, the unit normal vectors of the tooth surfaces including fillet surfaces of the rack-cutter can be obtained in the coordinate system s_n as:

$$\boldsymbol{n}_n^{pf-j}=\left|\frac{\partial \boldsymbol{R}_n^{pf-j}/\partial u)\times\partial \boldsymbol{R}_n^{pf-j}/\partial l)}{\partial \boldsymbol{R}_n^{pf-j}/\partial u)\times\partial \boldsymbol{R}_n^{pf-j}/\partial l)}\right|=\begin{bmatrix}+\sin\alpha_n\\ -\cos\alpha_n\\ 0\end{bmatrix}(j=l,r) \tag{6}$$

$$\boldsymbol{n}_n^{cf-j}(\theta)=\left|\frac{\partial \boldsymbol{R}_n^{cf-j}/\partial\theta)\times\partial \boldsymbol{R}_n^{cf-j}/\partial l)}{\partial \boldsymbol{R}_n^{cf-j}/\partial\theta)\times\partial \boldsymbol{R}_n^{cf-j}/\partial l)}\right|=\begin{bmatrix}+\cos\theta\\ -\sin\theta\\ 0\end{bmatrix}(j=l,r) \tag{7}$$

Fig. 3 shows the enveloping motion relation. During the enveloping, the rack-cutter moves along the direction of the axis y_c. At the same time, the to-be-generated beveloid gear rotates along the self-axis. According to the geometric relationship and enveloping motion, the homogeneous coordinate transformation matrices among the coordinate system can be obtained as:

$$M_{pn}=\begin{bmatrix}1&0&0&0\\0&\cos\beta&\sin\beta&0\\0&-\sin\beta&\cos\beta&0\\0&0&0&1\end{bmatrix}M_{cp}=\begin{bmatrix}\cos\delta&0&\sin\delta&0\\0&1&0&0\\-\sin\delta&0&\cos\delta&0\\0&0&0&1\end{bmatrix} \tag{8}$$

$$M_{fc}(\varphi_g)=\begin{bmatrix}1&0&0&r_g\\0&1&0&r_g\varphi_g\\0&0&1&0\\0&0&0&1\end{bmatrix}M_{gf}(\varphi_g)=\begin{bmatrix}\cos\varphi_g&\sin\varphi_g&0&0\\-\sin\varphi_g&\cos\varphi_g&0&0\\0&0&1&0\\0&0&0&1\end{bmatrix} \tag{9}$$

The geometry of the to-be-generated beveloid gear's tooth surfaces is obtained as the envelope to the family of the rack-cutter in the coordinate system s_g, represented as:

$$\boldsymbol{R}_g^{pf-j}(u,l,\varphi_g)=\boldsymbol{M}_{gf}(\varphi_g)\boldsymbol{M}_{fc}(\varphi_g)\boldsymbol{M}_{cp}\boldsymbol{M}_{pn}\boldsymbol{R}_n^{pf-j}(u,l)\ (j=l,r) \tag{10}$$

$$\boldsymbol{R}_g^{cf-j}(\theta,l,\varphi_g)=\boldsymbol{M}_{gf}(\varphi_g)\boldsymbol{M}_{fc}(\varphi_g)\boldsymbol{M}_{cp}\boldsymbol{M}_{pn}\boldsymbol{R}_n^{cf-j}(\theta,l)\ (j=l,r) \tag{11}$$

In the coordinate system s_g, the normal vectors of the rack-cutter can be obtained as:

$$\boldsymbol{n}_g^{pf-j}(\varphi_g)=\boldsymbol{L}_{gf}(\varphi_g)\boldsymbol{L}_{fc}(\varphi_g)\boldsymbol{L}_{cp}\boldsymbol{L}_{pn}\boldsymbol{n}_n^{pf-j}\ (j=l,r) \tag{12}$$

$$\boldsymbol{n}_g^{cf-j}(\varphi_g,\theta)=\boldsymbol{L}_{gf}(\varphi_g)\boldsymbol{L}_{fc}(\varphi_g)\boldsymbol{L}_{cp}\boldsymbol{L}_{pn}\boldsymbol{n}_n^{cf-j}(\theta)\ (j=l,r) \tag{13}$$

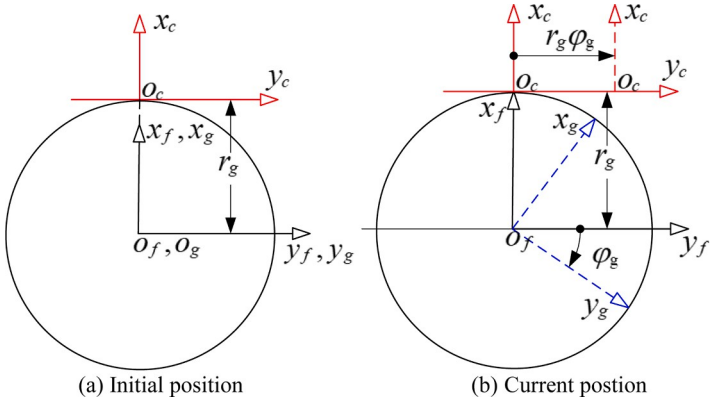

Fig. 3. Position of rack cutter and to-be-generated beveloid gear [32].

where $\boldsymbol{L}_{gf}$, $\boldsymbol{L}_{fc}$, $\boldsymbol{L}_{cp}$ and $\boldsymbol{L}_{pn}$ are the upper left three dimensional submatrices of $\boldsymbol{M}_{gf}$, $\boldsymbol{M}_{fc}$, $\boldsymbol{M}_{cp}$, and $\boldsymbol{M}_{pn}$ respectively.

The determination of the geometry of the to-be-generated beveloid gear is based on the simultaneous consideration of Eq(10–11) and the meshing equations. According to the gearing theory [33], the meshing equations can be expressed as:

$$f_{pg}^{j}(u,l,\varphi_g) = \left(\frac{\partial \boldsymbol{R}_g^{pf-j}}{\partial u} \times \frac{\partial \boldsymbol{R}_g^{pf-j}}{\partial l}\right) \frac{\partial \boldsymbol{R}_g^{pf-j}}{\partial \varphi_g} = 0 \ (j=l,r) \tag{14}$$

$$f_{cg}^{j}(\theta,l,\varphi_g) = \left(\frac{\partial \boldsymbol{R}_g^{cf-j}}{\partial \theta} \times \frac{\partial \boldsymbol{R}_g^{cf-j}}{\partial l}\right) \frac{\partial \boldsymbol{R}_g^{cf-j}}{\partial \varphi_g} = 0 \ (j=l,r) \tag{15}$$

here

$$\left(\frac{\partial \boldsymbol{R}_g^{pf-j}}{\partial u} \times \frac{\partial \boldsymbol{R}_g^{pf-j}}{\partial l}\right) = \boldsymbol{n}_g^{pf-j}(\varphi_g) \tag{16}$$

$$\left(\frac{\partial \boldsymbol{R}_g^{cf-j}}{\partial \theta} \times \frac{\partial \boldsymbol{R}_g^{cf-j}}{\partial l}\right) = \boldsymbol{n}_g^{cf-j}(\varphi_g,\theta) \tag{17}$$

$$\frac{\partial \boldsymbol{R}_g^{pf-j}}{\partial \varphi_g} = \frac{\partial \boldsymbol{M}_{gf}}{\partial \varphi_g}\boldsymbol{M}_{fc}\boldsymbol{M}_{cp}\boldsymbol{M}_{pn}\boldsymbol{R}_n^{pf-j} + \boldsymbol{M}_{gf}\frac{\partial \boldsymbol{M}_{fc}}{\partial \varphi_g}\boldsymbol{M}_{pn}\boldsymbol{R}_n^{pf-j} \ (j=l,r) \tag{18}$$

$$\frac{\partial \boldsymbol{R}_g^{cf-j}}{\partial \varphi_g} = \frac{\partial \boldsymbol{M}_{gf}}{\partial \varphi_g}\boldsymbol{M}_{fc}\boldsymbol{M}_{cp}\boldsymbol{M}_{pn}\boldsymbol{R}_n^{cf-j} + \boldsymbol{M}_{gf}\frac{\partial \boldsymbol{M}_{fc}}{\partial \varphi_g}\boldsymbol{M}_{pn}\boldsymbol{R}_n^{cf-j} \ (j=l,r) \tag{19}$$

where

$$\frac{\partial M_{gf}(\varphi_g)}{\partial \varphi_g} = \begin{bmatrix} -\sin\varphi_g & \cos\varphi_g & 0 & 0 \\ -\cos\varphi_g & -\sin\varphi_g & 0 & 0 \\ 0 & 0 & 0 & 0 \\ 0 & 0 & 0 & 0 \end{bmatrix} \frac{\partial M_{fc}(\varphi_g)}{\partial \varphi_g} = \begin{bmatrix} 0 & 0 & 0 & 0 \\ 0 & 0 & 0 & r_g \\ 0 & 0 & 0 & 0 \\ 0 & 0 & 0 & 0 \end{bmatrix} \tag{20}$$

Based on the simultaneous consideration of Eq(10–11) and Eq(14–15), the geometry of to-be-generated beveloid gear's tooth with the fillet can be obtained as:

$$\begin{cases} \boldsymbol{R}_g^{pf-j}(u,l,\varphi_g) = \boldsymbol{M}_{gf}(\varphi_g)\boldsymbol{M}_{fc}(\varphi_g)\boldsymbol{M}_{cp}\boldsymbol{M}_{pn}\boldsymbol{R}_n^{pf-j}(u,l) \\ f_{pg}(u,l,\varphi_g) = \left(\frac{\partial \boldsymbol{R}_g^{pf-j}}{\partial u} \times \frac{\partial \boldsymbol{R}_g^{pf-j}}{\partial l}\right) \frac{\partial \boldsymbol{R}_g^{pf-j}}{\partial \varphi_g} = 0 \end{cases} (j=l,r) \tag{21}$$

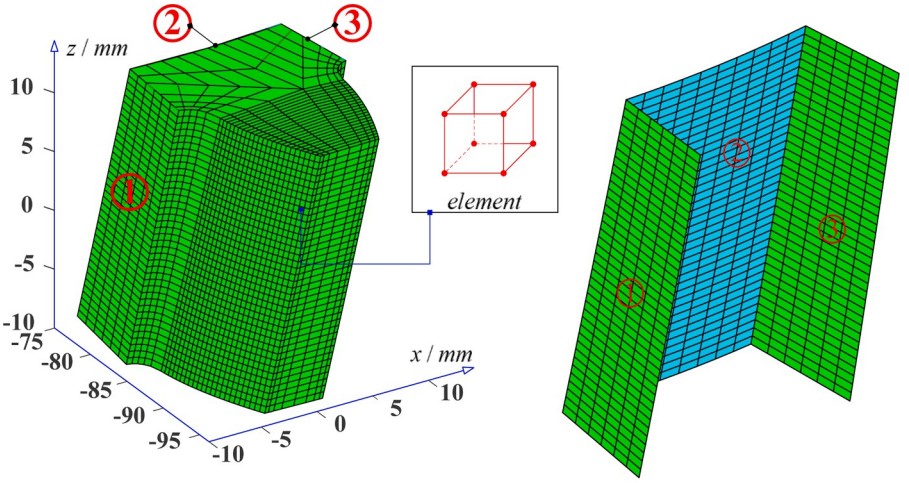

(a) Finite element modeling (b) Boundary constraint

Fig. 4. Finite element modeling and boundary constraint.

$$\begin{cases} \boldsymbol{R}_g^{cf-j}(\theta, l, \varphi_g) = \boldsymbol{M}_{gf}(\varphi_g)\boldsymbol{M}_{fc}(\varphi_g)\boldsymbol{M}_{cp}\boldsymbol{M}_{pn}\boldsymbol{R}_n^{cf-j}(\theta, l) \\ f_{jg}(\theta, l, \varphi_g) = \left(\dfrac{\partial \boldsymbol{R}^{cf-j}}{\partial \theta} \times \dfrac{\partial \boldsymbol{R}^{cf-j}}{\partial l}\right) \dfrac{\partial \boldsymbol{R}^{cf-j}}{\partial \varphi_g} = 0 \end{cases} \quad (j = l, r) \tag{22}$$

2.2. Flexibility determination of beveloid gears

2.2.1. FE model of beveloid gears and boundary condition

During the transmission of crossed beveloid gears, there is complex deformation in the contact tooth surfaces, which includes gear blank deflection, bending defection, shear deflection and contact deformation. Considering that there is no universal analytical method to calculate the bending deformation and shear deflection for beveloid gears, FEM is applied to calculate the comprehensive deformation. Hexahedral isoparametric element with 8 nodes is chosen.

The mesh grids of the tooth surfaces, including the root fillet surfaces, can be derived by meshing the rack-cutter parameters, according to Eq(21–22). The number of nodes in the other structure is also set. The tooth surfaces have thicker mesh grids to ensure the accuracy of the results. A gradual adjustment in the length of an element is performed at the same time. Generally speaking, the closer to the tooth surface, the higher the grid node density [9,34]. In the direction of the tooth width, the length of an element is set equal. Fig. 4(a) represents the finite element modeling.

Here, the area 1, 2 and 3 are the parts excluding the tooth surfaces and fillet surfaces extracted from the tooth structure, as shown in Fig. 4(b). All the degrees of freedom of all nodes in these areas are constrained.

2.2.2. Determination of flexibility for any point at the tooth surfaces

Based on the element type and finite element theory [35], the stiffness matric of a single element can be expressed as:

$$\boldsymbol{k}^e = \int_V \int \int \boldsymbol{B}^T \boldsymbol{D} \boldsymbol{B} |\boldsymbol{J}| d\xi d\eta d\zeta \tag{23}$$

where v represents the integration region. Since the integration variables are ξ, η and ζ, which are in isoperimetric element coordinates, v is the cubic space. The upper and lower bounds of the integration variables ξ, η and ζ are from —1 to 1. $\boldsymbol{B}$ is geometric matrix and $\boldsymbol{J}$ is the Jacobin matrix [36]. Here, $\boldsymbol{B}$ can be expressed as:

$$[\boldsymbol{B}] = [\boldsymbol{B}_1 \quad \boldsymbol{B}_2 \quad \boldsymbol{B}_3 \quad \boldsymbol{B}_4 \quad \boldsymbol{B}_5 \quad \boldsymbol{B}_6 \quad \boldsymbol{B}_7 \quad \boldsymbol{B}_8] \tag{24}$$

Further, the submatrices $\boldsymbol{B}_i$ can be represented as:

$$B_i = \begin{bmatrix} \partial N_i/\partial x & 0 & 0 \\ 0 & \partial N_i/\partial y & 0 \\ 0 & 0 & \partial N_i/\partial z \\ \partial N_i/\partial y & \partial N_i/\partial x & 0 \\ 0 & \partial N_i/\partial z & \partial N_i/\partial y \\ \partial N_i/\partial z & 0 & \partial N_i/\partial x \end{bmatrix} (i = 1, 2, \cdots, 8) \tag{25}$$

where N_i is the shape function and can be obtained in the reference [35,36]. x, y and z are the coordinates of the element in the local coordinate system.

Applying B-Bar method [37], $\boldsymbol{k}^e$ can be calculated accurately. By assembling the elements' stiffness matrices, the global stiffness matrix $\boldsymbol{K}$ of the single tooth structure can be obtained. Considering the boundary condition shown in Fig. 4(b), where all freedom degrees of the corresponding nodes are fixed and the displacements are 0, we delete the all rows and columns corresponding with the constrained nodes of the global stiffness matrix $\boldsymbol{K}$. For any node in the tooth surfaces, the force vector can be expressed as:

$$\boldsymbol{F}_j = [F_{jx} \quad F_{jy} \quad F_{jz}] \tag{26}$$

where j is the number of the node. F_{jx}, F_{jy} and F_{jz} represent the force along the axis x, y and z in the local coordinate system respectively. Assembling the all nodes' force, we can obtain force vector $\boldsymbol{F}$.

According to the following equation the deformations of all nodes can be obtained.

$$\boldsymbol{F} = \boldsymbol{K}\boldsymbol{\gamma} \tag{27}$$

For the above formulation, the global stiffness matrix $\boldsymbol{K}$ is save as sparse matrix and cholesky decomposition is applied to the global stiffness matrix $\boldsymbol{K}$ for solving Eq.(27). Taking the node j for example, giving the unit force along axis x, y and z respectively, we can obtain the deformations of all nodes under the unit force along corresponding directions. Further, we can extract the deformations of the nodes in the tooth surfaces, which can be denoted as $\boldsymbol{\gamma}_j^x$, $\boldsymbol{\gamma}_j^y$ and $\boldsymbol{\gamma}_j^z$. Parameter $\boldsymbol{\gamma}_j^x$ is

$$\boldsymbol{\gamma}_j^x = \begin{bmatrix} [\quad] & [\quad] & \cdots & [\quad] \\ \boldsymbol{\gamma}_{1-j}^x{}_{1\times 3} & \boldsymbol{\gamma}_{2-j}^x{}_{1\times 3} & & \boldsymbol{\gamma}_{n-j}^x{}_{1\times 3} \end{bmatrix} \tag{28}$$

here

$$\left[\boldsymbol{\gamma}^{x}_{1-j}\right]_{1\times 3} = \left[\gamma^{x-x}_{1-j} \quad \gamma^{x-y}_{1-j} \quad \gamma^{x-z}_{1-j}\right] \tag{29}$$

where γ^{x-x}_{1-j} represents the deformation along axis x of the node 1 under the condition where the unit force along axis x of node j is performed. Further, the deformations of all nodes in the tooth surfaces can be extracted, which constitute the flexibility matrix of the nodes in the tooth surfaces. By changing the nodes applied the force, we can obtain the flexibility matrix. It is worth noting that the deformation based on Eq(27) is the comprehensive deformation, which includes the bending deformation, shear deflection.

For any point τ in the tooth surfaces that is not a node, the force $\boldsymbol{F}_\tau$ applied in the point can be equivalent to the eight nodes at the tooth surfaces surrounding it, just as shown in Fig. 5. According to the virtual work theory, the equivalent force can be expressed as:

$$\boldsymbol{F}_{ei} = N_i(\xi,\eta,\zeta)\boldsymbol{F}_\tau \ (i = j_1, j_2, \cdots, s_4) \tag{30}$$

Because the point is more closed to the node j_1, j_2, j_3 and j_4 which are the nodes in the tooth surfaces, N_{j_1}, N_{j_2}, N_{j_3} and N_{j_4} are significantly greater than N_{s_1}, N_{s_2}, N_{s_3} and N_{s_4}. Therefore, the equivalent force at the node s_1, s_2, s_3 and s_4 is ignored in the paper.

Fig5. Equivalent force calculation

After obtaining the equivalent force at the four nodes surrounding the point, the deformations at all nodes in the tooth surfaces can be obtained by overlapping the deformations resulting from the equivalent forces, which can be obtained as:

$$\gamma_\tau = \sum_i \sum_j \boldsymbol{\gamma}^{j}_{i} F^{j}_{i} \ (i = j_1, j_2, j_3, j_4; j = x, y, z) \tag{31}$$

All above derivation can be used to calculate the deformations at the nodes. For the deformations at the point that is not the node, the interpolation method is applied [38]. According to the deformations at the nodes, we can obtain the interpolant between deformation and the generating parameter u and l, which can be denoted as:

$$\gamma^{x}_{\tau}(u,l) = \begin{bmatrix} f^{x-x}_{\tau}(u,l) \\ f^{x-y}_{\tau}(u,l) \\ f^{x-z}_{\tau}(u,l) \end{bmatrix} \tag{32}$$

where $f^{x-x}_{\tau}(u,l)$ represent the interpolant between the deformation along the axis x and the generating parameter u and l, when an unit force along the axis x is applied on the point τ.

3. Solving model of contact pressure for crossed beveloid gears

3.1. Tooth contact point determination and separation calculation

3.1.1. Determine tooth contact point

The tooth contact point is very critical to determine the contact pattern and other evaluation items [39–41]. According to the installation relationship, a transmission model of crossed beveloid gears is established, just as illustrated in Fig. 6. Here, four coordinate systems s_f, s_1, s_p and s_g. are introduced. Among them, the coordinate systems s_f and s_1 are reference coordinate systems. The coordinate systems s_p and s_g are rigidly connected to the pinion and gear. The parameters E, Σ, d_1 and d_2 are the installation parameters [42,43].

According to the geometrical relationship, the homogeneous transformation matrices between the coordinate system are:

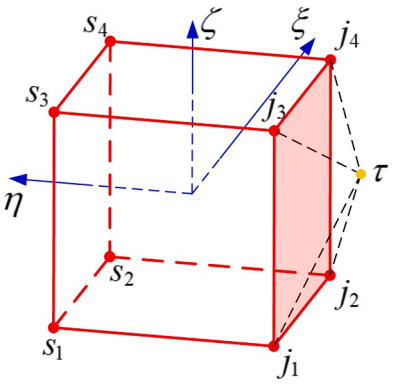

Fig. 5. Equivalent force calculation.

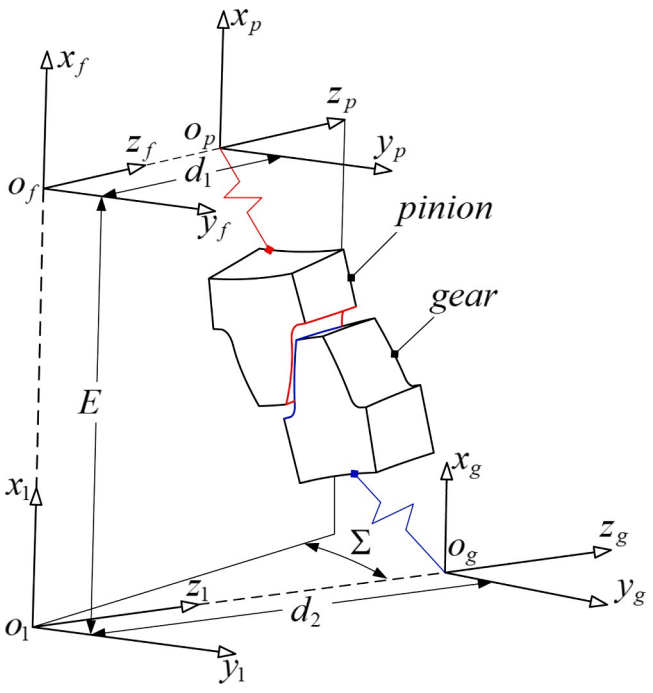

Fig. 6. Meshing model of crossed beveloid gears.

$$M_{fp} = \begin{bmatrix} \cos\phi_p & \sin\phi_p & 0 & 0 \\ -\sin\phi_p & \cos\phi_p & 0 & 0 \\ 0 & 0 & 1 & d_1 \\ 0 & 0 & 0 & 1 \end{bmatrix} \quad M_{f1} = \begin{bmatrix} 1 & 0 & 0 & -E \\ 0 & \cos\Sigma & \sin\Sigma & 0 \\ 0 & -\sin\Sigma & \cos\Sigma & 0 \\ 0 & 0 & 0 & 1 \end{bmatrix}$$

$$M_{1g} = \begin{bmatrix} \cos\phi_g & -\sin\phi_g & 0 & 0 \\ \sin\phi_g & \cos\phi_g & 0 & 0 \\ 0 & 0 & 1 & d_2 \\ 0 & 0 & 0 & 1 \end{bmatrix} \tag{33}$$

In the coordinate system s_f, the geometry of the pinion and gear can be expressed as:

$$\boldsymbol{R}_f^{pf-j}(u_p, l_p, \varphi_p, \phi_p) = \boldsymbol{M}_{fp}(\phi_p)\boldsymbol{R}_g^{pf-j}(u_p, l_p, \varphi_p) \quad (j = l, r) \tag{34}$$

$$\boldsymbol{R}_f^{gf-j}(u_g, l_g, \varphi_g, \phi_g) = \boldsymbol{M}_{f1}\boldsymbol{M}_{1g}(\phi_g)\boldsymbol{R}_g^{pf-j}(u_g, l_g, \varphi_g) \quad (j = l, r) \tag{35}$$

The normal vectors of the tooth surfaces can be obtained in the coordinate system s_f as:

$$\boldsymbol{n}_f^{pf-j}(\varphi_p, \phi_p) = \boldsymbol{L}_{fp}(\phi_p)\boldsymbol{n}_g^{pf-j}(\varphi_p) \quad (j = l, r) \tag{36}$$

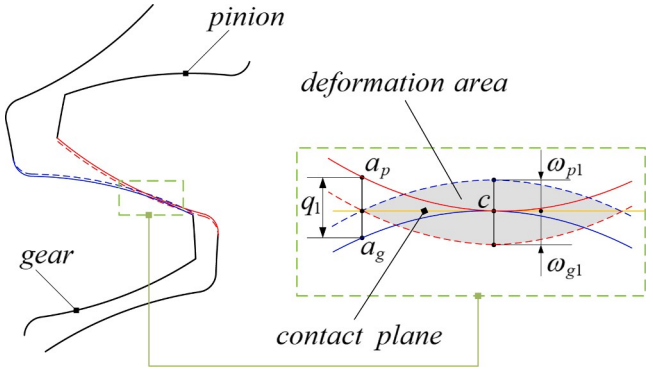

Fig. 7. Contact of tooth pairs under load.

$$\boldsymbol{n}_f^{gf-j}\left(\varphi_g, \phi_g\right) = \boldsymbol{L}_{f1}\boldsymbol{L}_{1g}\left(\phi_g\right)\boldsymbol{n}_g^{pf-j}\left(\varphi_g\right) \quad (j = l, r) \tag{37}$$

According to the gearing theory [33], the contact point meets the following condition:

$$\begin{cases} R_f^{pf-j}\left(u_p, l_p, \varphi_p, \phi_p\right) = R_f^{gf-j}\left(u_g, l_g, \varphi_g, \phi_g\right) \quad (j = l, r) \\ n_f^{pf-j}\left(\varphi_p, \phi_p\right) = -n_f^{gf-j}\left(\varphi_g, \phi_g\right) \quad (j = l, r) \end{cases} \tag{38}$$

This is a vector equation consisting of 6 equations and 8 variables. Because $\boldsymbol{n}_f^{pf-j}$ and $\boldsymbol{n}_f^{gf-j}$ are unit vectors, it only includes 5 independent equations. Combining with Eq(21), if ϕ_p or ϕ_g is given, Eq(38) can be solved.

3.2. Solving model of contact pressure

3.2.1. Deformation compatibility

A contact model of a tooth pair under load is shown in Fig. 7. Here, the point c is the contact point. Under the load, there are elastic deformations in the contact pair and the contact area is extended from a point to a plane. The deformation amounts of the contact pair are ω_{p1} and ω_{g1}, which brings the point a_p and a_g, of which the separation is q_1, into contact.

As the initial contact point, the deformations amount of the point c at the tooth surfaces are maximum. Therefore, the total maximum deformation can be expressed:

$$\omega_m = \omega_{p1} + \omega_{g1} \tag{39}$$

Considering the total deformation, we can obtain that the points which is under the contact area meet the following condition:

$$q + \omega_p + \omega_g = \omega_m \tag{40}$$

where q is the separation. ω_p and ω_g are the deformations of the point pair.

For the point pair, which are at the boundary of the contact area, the separation between them can be expressed:

$$q = \omega_m \tag{41}$$

3.2.2. Deformation calculation and model establishment

The contact deformation inside the contact region for the contact pair is in the normal direction of the contact point. Even though the other deformation may not be in the same direction, we continue to assume that the contact plane is a tangent plane. In the contact plane, we discretize the contact area into some rectangles with length A and width B, as illustrated in Fig. 8. Herein, a coordinate system s_c is introduced, of which the origin is the contact point c and the axis y_c coincides with the major axis of the contact ellipse. For any point i at the contact plane, it is constructed by the point p_{i-p} and p_{i-g}, which are at the surfaces of the pinion and gear respectively, and forms a contact point pair. According to the theory of the influence coefficient method, the deformation of any point in the contact area is caused by its own load and other points' load. For the contact segment i, the deformation amount can be expressed as:

$$\omega_i = \omega_{i-p} + \omega_{i-g} \tag{42}$$

where ω_i represents the total deformation amount of the segment i; ω_{i-p} and ω_{i-g} are the total deformations of the point p_{i-p} and p_{i-g}.

The deformation ω_{i-p}can be expressed as:

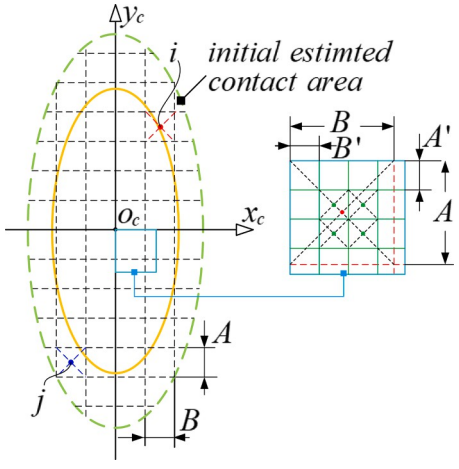

Fig. 8. Contact area.

$$\omega_{i-p} = \sum_{j=1} F_j c_{ij-p} \tag{43}$$

where c_{ij-p} is the deformation amount of the segment i along the common normal direction and caused by unit force of the segment j. F_j is the force in the segment j. According to Eq.(32), c_{ij-p} can be expressed as:

$$c_{ij-p} = \boldsymbol{n}_c^T \begin{bmatrix} f_{j-p}^{x-x}(u_i, l_i) & f_{j-p}^{y-x}(u_i, l_i) & f_{j-p}^{z-x}(u_i, l_i) \\ f_{j-p}^{x-y}(u_i, l_i) & f_{j-p}^{y-y}(u_i, l_i) & f_{j-p}^{z-y}(u_i, l_i) \\ f_{j-p}^{x-z}(u_i, l_i) & f_{j-p}^{y-z}(u_i, l_i) & f_{j-p}^{z-z}(u_i, l_i) \end{bmatrix} \boldsymbol{n}_c \tag{44}$$

where $\boldsymbol{n}_c$ is the normal vector of the contact point in the local system. u_i and l_i are the generating parameters of the point p_{i-p}. Applying the same method, ω_{i-p} and c_{ij-g} can be obtained. F_j can be represented as:

$$F_j = \rho_j s \tag{45}$$

where ρ_j is the average pressure on the rectangle area j and s is the area of the segment. The total load in the contact area is the transmitted torque, which can be expressed as:

$$T = \sum_{j=1} v_j F_j \tag{46}$$

where T is the transmitted torque and v_j is the torque generated by unit force of the segment j and can be expressed as:

$$v_j = \boldsymbol{n}_c^f \times \boldsymbol{r}_f^j \tag{47}$$

here $\boldsymbol{r}_f^j$ is the position vector of the point p_j in the coordinate system s_f.

Combining with deformation compatibility, the force and deformation of all segments meet the following formulation:

$$\begin{aligned} &(c_{11-p} + c_{11-g})F_1 + \cdots (c_{1j-p} + c_{1j-g})F_j + \cdots (c_{1n-p} + c_{1n-g})F_n = \omega_m - q_1 \\ &\qquad\qquad \vdots \; \vdots \; \vdots \; \vdots \\ &(c_{j1-p} + c_{j1-g})F_1 + \cdots (c_{jj-p} + c_{jj-g})F_j + \cdots (c_{jn-p} + c_{jn-g})F_n = \omega_m - q_j \\ &\qquad\qquad \vdots \; \vdots \; \vdots \; \vdots \\ &(c_{n1-p} + c_{n1-g})F_1 + \cdots (c_{nj-p} + c_{nj-g})F_j + \cdots (c_{nn-p} + c_{nn-g})F_n = \omega_m - q_n \\ &v_1F_1 + \cdots v_jF_j + \cdots v_nF_n = T \end{aligned} \tag{48}$$

The above formulation can be rewritten as matrix form as:

$$\begin{bmatrix} \boldsymbol{c}_{n\times n} & \boldsymbol{I}_{n\times 1} \\ \boldsymbol{v}_{1\times n} & 0 \end{bmatrix} \begin{bmatrix} \boldsymbol{F}_{n\times 1} \\ -\omega_m \end{bmatrix} = \begin{bmatrix} -\boldsymbol{q}_{n\times 1} \\ T \end{bmatrix} \tag{49}$$

here $\boldsymbol{c}_{n\times n}$ is the deformation coefficient matrix and can be expressed as:

$$\boldsymbol{c}_{n\times n} = \begin{bmatrix} c_{11-p} + c_{11-g} & \cdots & c_{1j-p} + c_{1j-g} & \cdots & c_{1n-p} + c_{1n-g} \\ \vdots & & \vdots & & \vdots \\ c_{j1-p} + c_{j1-g} & \cdots & c_{jj-p} + c_{jj-g} & \cdots & c_{jn-p} + c_{jn-g} \\ \vdots & & \vdots & & \vdots \\ c_{n1-p} + c_{n1-g} & \cdots & c_{nj-p} + c_{nj-g} & \cdots & c_{nn-p} + c_{nn-g} \end{bmatrix} \tag{50}$$

where $\boldsymbol{v}_{1\times n}$ and $\boldsymbol{q}_{n\times 1}$ represent the vectors comprised by torque coefficients and the separation. $\boldsymbol{I}_{n\times 1}$ is the $n \times 1$ unit matrix.

3.2.3. Initial contact area setting and solving method

Eq.(48) is a system of $n + 1$-order linear equation. It is worth noting that $\boldsymbol{c}_{n\times n}$ is a deformation coefficient matrix and the value of each element is influenced by the elastic modulus of the material. In engineering, the elastic modulus of common gear materials usually is above $200GPa$, which result in the elements of $\boldsymbol{c}_{n\times n}$ of order of magnitude of 10^{-6}. Therefore, there is obvious order of magnitude difference in the coefficient matrix. It will cause the coefficient matrix of Eq.(48) ill-conditioned.

For the influence coefficient method, the average contact pressure is calculated. To calculate the exact contact pressure, the dimensions of the segments need to be decreased, which lead to very dense segments and enlarge the order of Eq.(48). It has the negative influence on the coefficient matrix's ill-conditioned.

Based on the above analysis, the following two strategies are applied. Firstly, more accurate initial contact area is estimated. In reference [25,44], the initial contact area is an overestimated rectangle area, which causes higher order of the coefficient matrix. In this study, the initial contact area is set as an ellipse. The length of major axis can be set as the tooth width. The length of minor axis can

be estimated according to the ratio of lengths of contact ellipse's major and minor axis. The ratio can be obtained based on the gearing theory [33].

At the basis of initial contact area estimation, preconditioning strategy is applied. Considering that the ill-conditioned of the coefficient matrix is caused by the difference in order of magnitude between $\boldsymbol{c}_{n\times n}$, $\boldsymbol{I}_{n\times 1}$ and $\boldsymbol{v}_{1\times n}$ to some extent. Firstly, the left preconditioner $\mathbf{L}$ is chosen, Eq.(48) can be rewritten as:

$$\mathbf{L}\begin{bmatrix}\boldsymbol{c}_{n\times n} & \boldsymbol{I}_{n\times 1}\\ \boldsymbol{v}_{1\times n} & 0\end{bmatrix}\begin{bmatrix}\boldsymbol{F}_{n\times 1}\\ -\omega_m\end{bmatrix}=\mathbf{L}\begin{bmatrix}-\boldsymbol{q}_{n\times 1}\\ T\end{bmatrix} \tag{51}$$

Through introducing $\mathbf{L}$, the order of magnitude of the last row of the coefficient matrix is adjusted to the same order of magnitude as $\boldsymbol{c}_{n\times n}$. Therefore, $\mathbf{L}$ can be expressed as:

$$\mathbf{L}=\begin{bmatrix}\boldsymbol{I}_{n\times n} & 0\\ 0 & L\end{bmatrix} \tag{52}$$

where L is chosen according to the difference of order of magnitude between $\boldsymbol{c}_{n\times n}$ and $\boldsymbol{v}_{1\times n}$.

Furthermore, the right preconditioner $\mathbf{R}$ is chosen. Eq.(51) can be further rewritten as:

$$\mathbf{L}\begin{bmatrix}\boldsymbol{c}_{n\times n} & \boldsymbol{I}_{n\times 1}\\ \boldsymbol{v}_{1\times n} & 0\end{bmatrix}\mathbf{R}\left(\mathbf{R}^{-1}\begin{bmatrix}\boldsymbol{F}_{n\times 1}\\ -\omega_m\end{bmatrix}\right)=\mathbf{L}\begin{bmatrix}-\boldsymbol{q}_{n\times 1}\\ T\end{bmatrix} \tag{53}$$

Through introducing $\mathbf{R}$, the order of magnitude of the last column of the coefficient matrix is adjusted to the same order of magnitude as $\boldsymbol{c}_{n\times n}$. Therefore, $\mathbf{R}$ can be expressed as:

$$\mathbf{R}=\begin{bmatrix}\boldsymbol{I}_{n\times n} & 0\\ 0 & R\end{bmatrix} \tag{54}$$

where R is chosen according to the difference of order of magnitude between $\boldsymbol{c}_{n\times n}$ and $\boldsymbol{I}_{n\times 1}$.

Through introducing the left and right preconditioner, the obvious difference of order of magnitude in the coefficient matrix is decreased, which increase the robustness of the solution.

After the preconditioning, the iteration method is applied to solving it. By the method of SVD, the equation can be solved. Moreover, the contact area is overestimated and extended to the boundary of the tooth surfaces at the beginning. Because of the overestimated contact area, there are some negative solutions, which is violation of contact theory. Therefore, the negative solutions are set 0 and the corresponding arear is not used in the next iteration. The procedure is repeated until all solutions are positive or 0 [25, 44]. It is worth noting that the contact area only is set before the solving and the to-be-determined contact area is changing with the iteration proceeding. The contact area is not determined until the iteration end.

3.4. Exact contact pressure and load distribution estimation

Only average contact pressure may be computed using the effect coefficient approach, which cannot match the demand for exact contact pressure in the contact point and maximum contact pressure. To accomplish this, the segments' lengths must be set to an infinitesimal value. The following three considerations, however, must not be ignored:

(a) With the length of the segments decreasing, the size of coefficient matrix is geometric progression growth, which will result in a significant increase in the condition number of the coefficient matrix. Further, the robustness of solution significantly decreases.
(b) With the length of the segments decreasing, the volatility of the solution increases significantly, which also lead a challenge in the estimation of exact contact pressure.
(c) It lacks an effective criterion to set the length and stop further subdividing the initial contact area to smaller segments.

In this study, a estimation method named numerical fitting method (NFM) of exact contact pressure is proposed. Here, we assume that the contact pressure is distributed as a quartic function on the contact plane, which can be expressed in coordinate system s_c as:

$$\begin{aligned}\mathrm{P}(x,y)=\ &a_0+a_1x+a_2y+a_3x^2+a_4xy+a_5y^2+a_6x^3+a_7x^2y+a_8xy^2+a_9y^3+a_{10}x^4+a_{11}x^3y+\\ &a_{12}xy^3+a_{13}x^2y^2+a_{14}y^4\end{aligned} \tag{55}$$

For the square segment with the origin as the center and length A, the average contact pressure can be expressed:

$$P_{ave}=\int_{-A/2}^{A/2}\int_{-A/2}^{A/2}\mathrm{P}(x,y)dxdy\Big/(A*A) \tag{56}$$

The above formulation can be simplified as:

$$P_{ave}=a_0+(a_3+a_5)A^2/12+((a_{10}+a_{14})/80+a_{13}/144)A^4 \tag{57}$$

where A^2 represents the area of the segment. Therefore, the average contact pressure is a quadratic function about the area. It is worth

noting that the constant term of the function is the exact contact pressure of the center of the segments. The coefficients of Eq (57) can be determined when the average contact pressures under the three kinds of dimensions′ segment. The above simplification is only obtained under the condition, where the segment is a square area with the same length and width.

For the other point in the contact area, when we choose the point as the origin to establish the contact pressure distribution, it can be obtained as:

$$\begin{aligned} P'(x,y) = {} & a'_0 + a'_1(x+\Delta x) + a'_2(y+\Delta y) + a'_3(x+\Delta x)^2 + a'_4(x+\Delta x)(y+\Delta y) + a'_5(y+\Delta y)^2 + \\ & a'_6(x+\Delta x)^3 + a'_7(x+\Delta x)^2(y+\Delta y) + a'_8(x+\Delta x)(y+\Delta y)^2 + a'_9(y+\Delta y)^3 + a'_{10}(x+\Delta x)^4 + \\ & a'_{11}(x+\Delta x)^3(y+\Delta y) + a'_{12}(x+\Delta x)(y+\Delta y)^3 + a'_{13}(x+\Delta x)^2(y+\Delta y)^2 + a'_{14}(y+\Delta y)^4 \end{aligned} \tag{58}$$

where Δx and Δy are the coordinates of the chosen point's coordinate in the coordinate system s_c. Because Δx and Δy are constants, Eq (59) is still a quartic function and Eq(57) can be also established in the chosen point.

According to Eq(57), the exact contact pressure of any point within the contact area can be estimated by selecting at least three kinds of segments with different dimension to calculate the average contact pressure and fitting the pressures and areas by quadratic function. However, the center points of the segments with different dimensions are not always the same, illustrated in Fig (8). Therefore, the fitting method based on a quartic function is applied to obtain the any point's contact pressure.

At the basis of obtaining sampling points′ exact contact pressure, the coefficients of Eq(55) can be determined. Further, the distribution of contact pressure can be obtained.

4. Numerical application example

A computer program was created to calculate the contact pressure and load distribution using the aforementioned derivation. The specifications of the beveloid gear pair and installation parameters are listed in Table 1. The same material is used each time. The elastic modulus is 206GPa and the Poisson ratio is 0.3. Two kinds of transmitted torque are tested, which are 100Nm and 300Nm.

The loaded tooth contact analysis using ABAQUS was used to test the correctness of the suggested approach. Solid models were originally built based on the specifications of the beveloid gears. Predetermined installation criteria were used to assemble the beveloid gear pair. Then, in ABAQUS, a finite element model was created, as shown in Fig. 9(a). A hexahedral grid was used as the mesh type. To ensure the balance between the high calculation efficiency and accuracy, the mesh in the contact tooth surfaces is denser. By adjusting the meshing parameters, a reliable simulation results were obtained, where the number of elements for the beveloid pinion was 131,502 and the number of elements for the beveloid gear was 118,863. The boundary condition is shown in Fig. 9(b). Here, beveloid pinion and gear are coupled on their coordinate systems respectively. During the simulation, a rotation angle is applied to the beveloid pinion, while a torque load is applied to the beveloid gear, so the analysis type is quasi-static [2].

Case1: 100Nm transmitted torque

In NFM, three kinds of the segment dimension are set, which are 0.3mm, 0.25mm and 0.2mm. FEM and NFM were used to obtain meshing point contact stress, maximum contact stress, and contact stress distribution. The contact pressures of contact areas and their distribution are shown in Fig. 10. There are two sorts of contact states found here. The first is overrun contact, which extends the contact region to the bounds of the tooth surfaces. Overrun contact occurs at the start or finish of a meshing operation. The other type of contact is common contact, in which the whole contact area is composed of tooth surfaces. In the contact plane, the distribution of contact stress is shown. The results show the contact stress of meshing points calculated by NFM keep good consistency with that from FEM during the common contact, where the maximum deviation between the two results is within 5%. At the same time, the shape and range of the contact stress distribution from the two methods are close to each other. However, the contact stresses of the minimal region near tooth surfaces′ bound are far more than that of other region in FEM. The phenomenon does not occur in NFM.

In the overrun contact, the contact pressures of meshing points increase obviously, which is account for decreasing contact area. The values from NFM are greater than that from FEM, the cause of which is that there is overrun contact in FEM. Under the condition that the transmitted torque is constant, the greater contact pressures under the region closed to the tooth surface bound generate more torque.

Furthermore, the maximum contact stresses are extracted, shown in Fig. 11. The results show that the maximum contact stresses

Table 1
Parameters of the beveloid gear pair.

Symbol		Unit	Pinon	Gear
Normal module	m_n	mm	2	2
Normal pressure angle	α_n	deg	20	20
Reference helix angle	β	deg	26.0902(LH)	16.6994(RH)
Cone angle	δ	deg	4	5
Number of teeth	Z		25	31
Tooth width	b	mm	20	20
Radius of root fillet		mm	0.5	0.5
Radius of shaft		mm	23	27
Crossing angle	Σ	deg	13	
Offset distance	d	mm	182.6570	182.3000
Center distance	E	mm	43.5332	

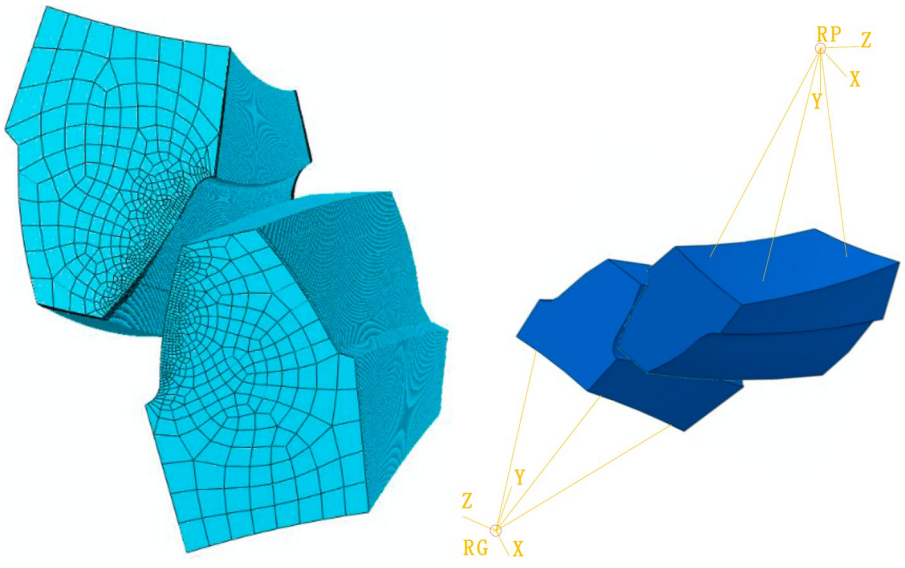

(a) Finite element model (b) Boundary condition

Fig. 9. Finite element model.

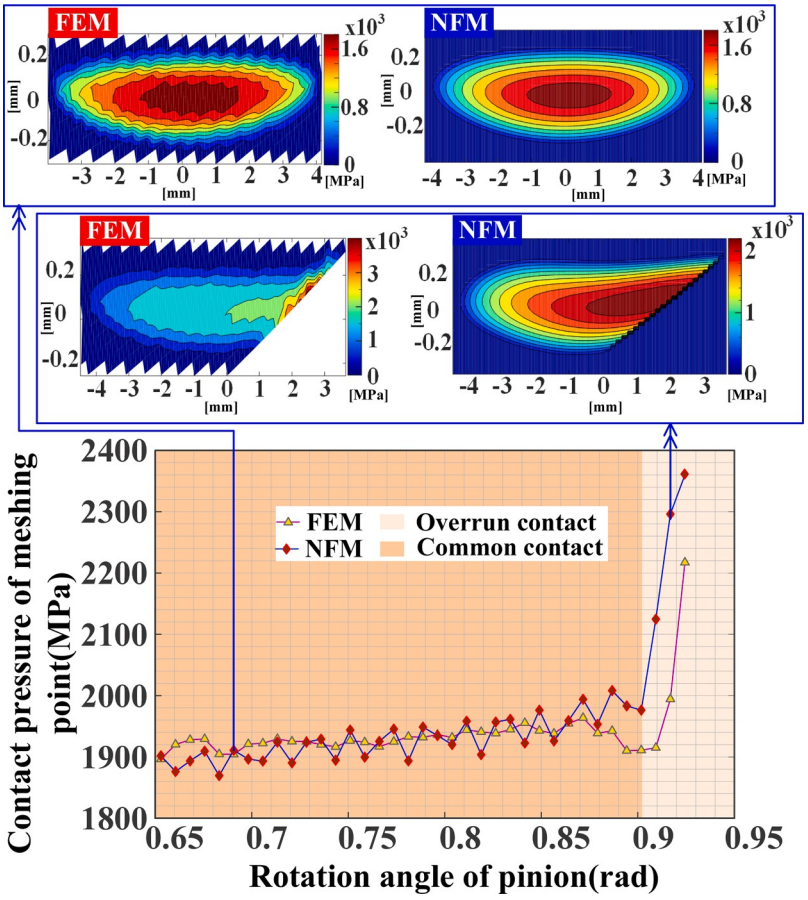

Fig. 10. Contact stress of meshing points and load distribution.

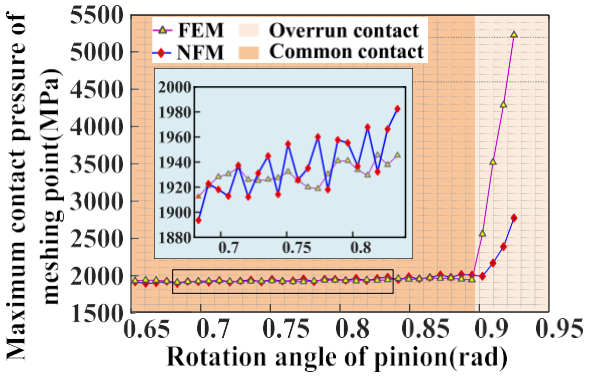

Fig. 11. Maximum contact pressure.

increase with the pinion rotation. The maximum contact stresses during the overrun contact are much greater than that in the common contact. It is worth noting that the maximum contact stresses calculated by the two methods are closed to each other during the common contact and the maximum deviation is no more than 4%.

Fig. 12 shows the contact pressure of the meshing point and the maximum contact pressure under the chosen length of the segment, when the rotation angle of the pinion is 0.6831 rad. Under the given meshing position, the contact pressure of the meshing point and maximum contact pressure from FEM are 1903.26 MPa and 1923.52 MPa. The results show that both the contact pressure of the meshing point and maximum contact pressure increase and the deviation between the estimation values and that from FEM decreases with the length of the segment decreasing. But the deviation still is obvious.

Case2: 300Nm transmitted torque

For NFM, the segment dimensions are 0.4mm, 0.3mm and 0.2mm. In Fig. 13, the contact pressure of meshing points and load distribution from FEM and NFM are shown. In comparison to Fig. 11, the dimensions of the contact area increase as the transmitted torque increases, resulting in overrun contact in the early stages of meshing. The results reveal that the contact pressures of meshing locations from FEM and NFM are nearly identical, with a maximum difference of 5%. The two results have similar overall tendencies. Despite the fact that the contact pressures in the region adjacent to the tooth surfaces bound are substantially higher than in other regions in FEM during overrun contact, the dimensions and form of the load distributions from both approaches maintain a high level of homogeneity.

Fig. 14 shows the maximum contact pressures from FEM and NFM. Here, the values from NFM increase with the pinion rotation. However, the curve representing the maximum contact pressures calculated by FEM is "U" shape. The maximum contact stresses during the overrun contact are much greater than that in the common contact. It is worth noting that the maximum contact stresses calculated by the two methods are closed to each other during the common contact and the maximum deviation is no more than 5% in the common contact.

Fig. 15 shows the contact pressure of the meshing point and the maximum contact pressure under the chosen length of the segment, when the rotation angle of the pinion is 0.6907 rad. Under the given meshing position, the contact pressure of the meshing point and maximum contact pressure from FEM are 2572.31 MPa and 2678.67 MPa. The calculation results keep the same trend as Fig. 12. The chosen lengths cannot estimate the contact pressure.

For the above numerical examples, the proposed method is less 4.2 h by 81.29% than FEM under the condition that the time

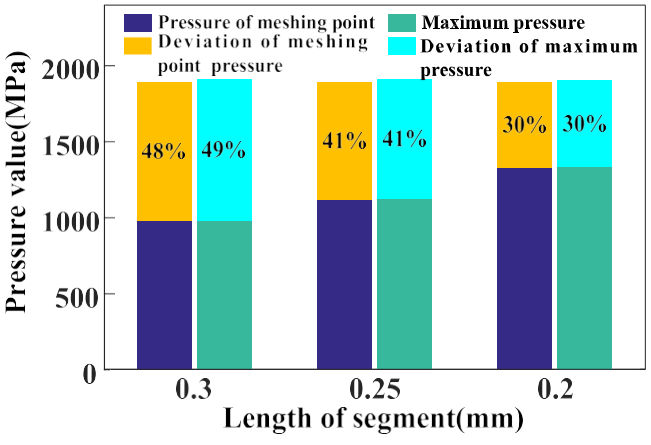

Fig. 12. Contact pressure under the given segment dimension with $\phi_p = 0.6831 rad$.

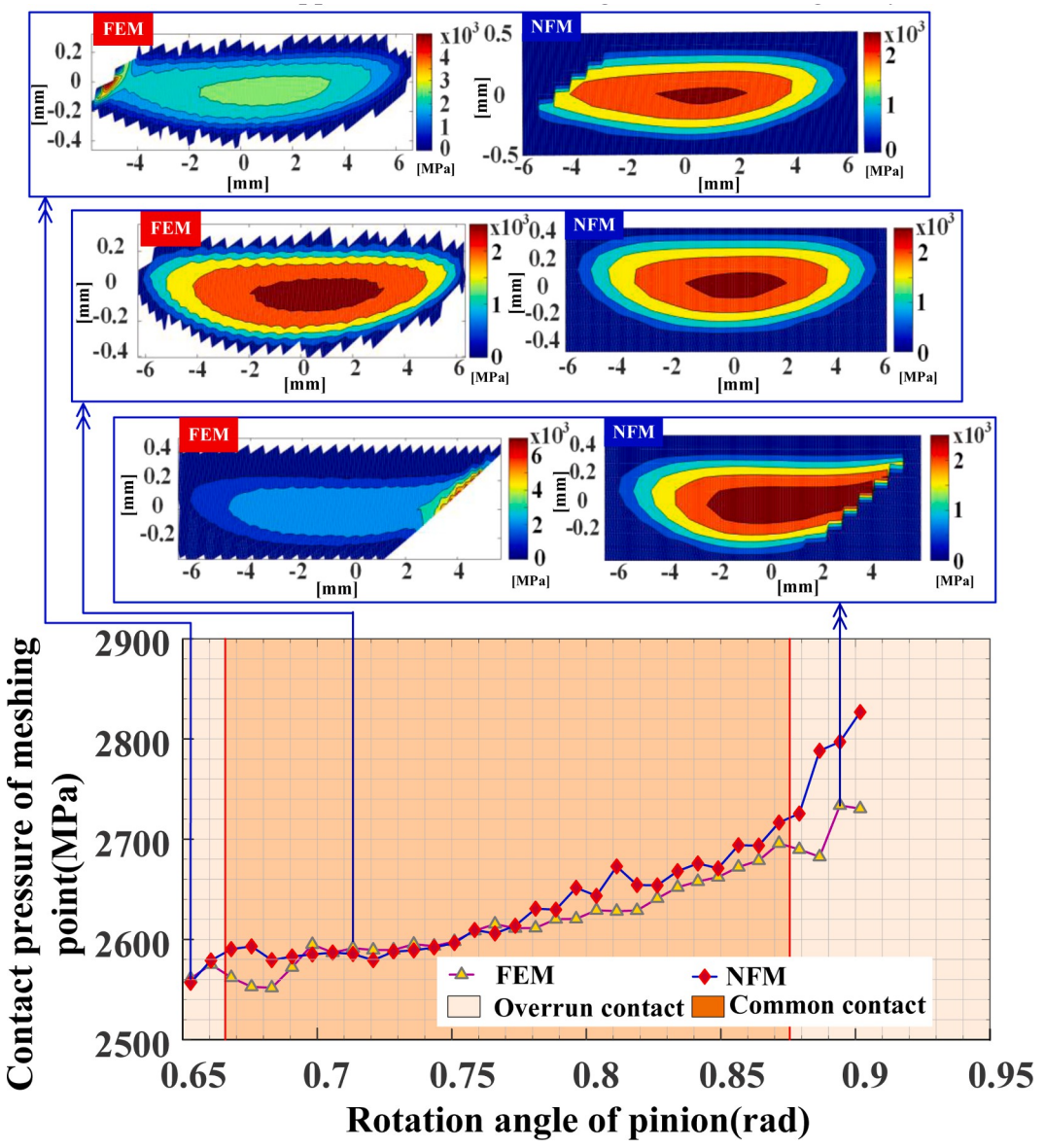

Fig. 13. Contact stress of meshing points and load distribution.

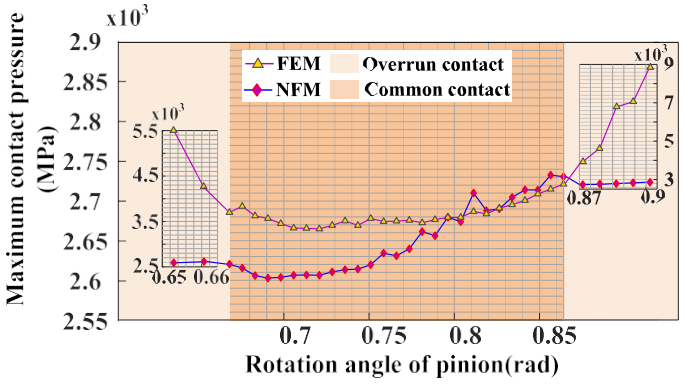

Fig. 14. Maximum contact stresses.

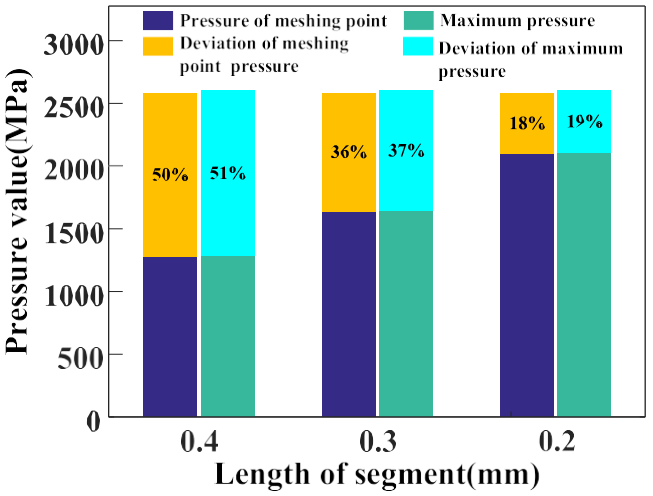

Fig. 15. Contact pressure under the given segment dimension with $\phi_p = 0.6907rad$.

required for developing 3D modeling, meshing, analysis settings and results analysis for FEM are not considered.

5. Discussion

For NFM, it is necessary to choose three kinds of dimensions of the segment for determining the exact contact pressure and load distribution. Here, the effect of the segment dimensions on the result is analyzed. The transmitted load is $300Nm$ and the rotation angle is $0.6907rad$. The contact pressure of the meshing point and the maximum contact pressure is shown in Fig. 16.

In this rotation angle, the contact pressure of meshing point and the maximum contact pressure from Abaqus are $2655MPa$ and $2678MPa$. We choose three sets of segment's dimensions. The results show that both Dimension2 and Dimension3 can achieve accurate estimation. However, the deviations between Dimension1 and the result from Abaqus are more than 10%. From Diemnsion1 to Diemnsion3, the maximum lengths of segments decrease and the estimation values from NFM are closer to the result from Abaqus.

According to Fig. 12, the half width of the contact area is about $0.4mm$. $0.5mm$ exceeds the limit of contact area, which causes the inaccurate estimation. Therefore, when choosing the maximum segment length, the range of contact area need to be considered. Moreover, as long as the condition is met, there is no other constraints for choosing other two segment length.

6. Conclusion

In this paper, a numerical method for estimating contact pressure and load distribution for crossed beveloid gears was proposed. Through a numerical example, the feasibility about the estimation of the contact stresses and load distribution during the common

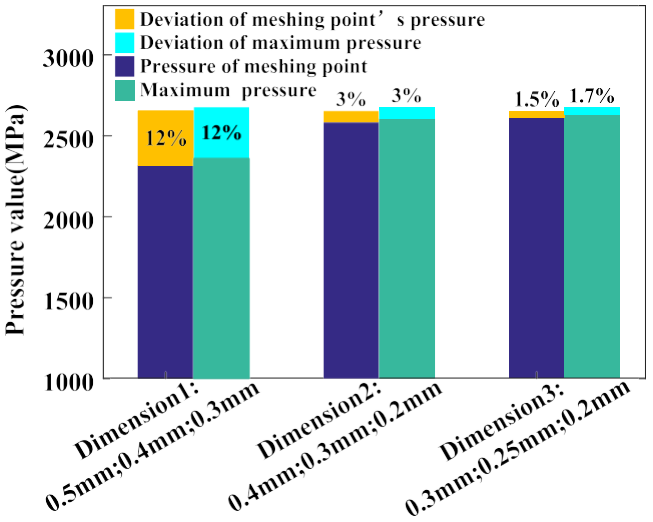

Fig. 16. Effect of segment’s dimension on the result.

contact was validated. Compared with the analysis based on ABAQUS, the proposed method improves computation efficiency more than 80%, which provides the basis for continuous improvement of crossed beveloid gears. The following aspects and conclusions can be summarized based on the above investigation:

1 An accurate beveloid gear teeth model with root fillets was established to obtain the force-displacement relation of contact points. All deformations are considered. A solving model of contact pressure was developed based on the influence coefficient method for the crossed beveloid gears.
2 Considering that the coefficient matrix of numerical solving model is ill-conditioned, two strategies including more accurate initial estimated contact area and preconditioning were applied to improve the robustness of the solution.
3 In view of the defects of the influence coefficient method that the dimensions of segments need to be infinitesimal to achieve the accurate estimation and there is not a criterion for choosing the dimensions of segments, a novel estimation method about exact contact stress was proposed. Moreover, the criterion to choose the segment length is established.

Declaration of Competing Interest

The authors declare that they have no known competing financial interests or personal relationships that could have appeared to influence the work reported in this paper.

Acknowledgments

The authors are grateful for support from the National Key Research and Development Plan (grant no. 2019YFB1703700), the National Natural Science Foundation, China (grant no. 51875066), the China Scholarship Council (grant no.202006050181) and the Chongqing special key project of technology innovation and application development(cstc2019jscx-mbdxX0034).

References

[1] H. Ding, J. Tang, Y. Zhou, J. Zhong, G. Wan, A multi-objective correction of machine settings considering loaded tooth contact performance in spiral bevel gears by nonlinear interval number optimization, Mech. Mach. Theory 113 (2017) 85–108.
[2] G. Ni, C. Zhu, C. Song, J. Shi, S. Liu, Effects of rack-cutter parabolic modification on loaded contact characteristics for crossed beveloid gears with misalignments, Int. J. Mech. Sci. 141 (2018) 359–371.
[3] C. Song, Y. Zhou, C. Zhu, G. Ni, S. Liu, Loaded tooth contact analysis of intersected beveloid and cylindrical involute gear pair with small shaft angle, J. Adv. Mech. Design, Syst. Manuf. 12 (2018). JAMDSM0004-JAMDSM0004.
[4] B. Cao, G. Li, Y. Tao, Q. Ran, Robust geometric parameter optimization of a crossed beveloid gear pair with approximate line contact, Mechanism and Machine Theory, 168 (2022) 104596.
[5] J. Bruyère, P. Velex, A simplified multi-objective analysis of optimum profile modifications in spur and helical gears,, Mech. Machine Theory 80 (2014) 70–83.
[6] V.V. Simon, Multi-objective optimization of hypoid gears to improve operating characteristics, Mech. Mach. Theory (2020) 146.
[7] H. Ding, J. Tang, J. Zhong, Accurate nonlinear modeling and computing of grinding machine settings modification considering spatial geometric errors for hypoid gears, Mech. Mach. Theory 99 (2016) 155–175.
[8] Q. Wang, C. Zhou, L. Gui, Z. Fan, Optimization of the loaded contact pattern of spiral bevel and hypoid gears based on a kriging model, Mech. Mach. Theory 122 (2018) 432–449.
[9] W. Qu, H. Ding, J. Tang, An innovative semi-analytical determination approach to numerical loaded tooth contact analysis (NLTCA) for spiral bevel and hypoid gears, Adv. Eng. Software (2020) 149.
[10] V. Simon, Load and stress distributions in spur and helical gears, J. Mech. Trans. Automation Design 110 (1988) 197–202.
[11] V. Simon, Load distribution in hypoid gears, J. Mech. Design 122 (1998) 529–535.
[12] V. Simon, Optimal machine tool setting for hypoid gears improving load distribution, J. Mech. Design 123 (2000) 577–582.
[13] V. Simon, FEM stress analysis in hypoid gears, Mechanism and Machine Theory, 35 (2000) 1197–1220.
[14] Y. Zhang, Z. Fang, Analysis of tooth contact and load distribution of helical gears with crossed axes, Mechanism and Machine Theory, 34 (1999) 41–57.
[15] X. Hou, Z. Fang, X. Zhang, Static contact analysis of spiral bevel gear based on modified VFIFE (vector form intrinsic finite element) method, Appl. Math Model 60 (2018) 192–207.
[16] J.I. Pedrero, I.I. Vallejo, M. Pleguezuelos, Calculation of tooth bending strength and surface durability of high transverse contact ratio spur and helical gear drives, J. Mech. Design 129 (2007) 69–74.
[17] M.B. Sánchez, J.I. Pedrero, M. Pleguezuelos, Contact stress calculation of high transverse contact ratio spur and helical gear teeth, Mech. Mach. Theory 64 (2013) 93–110.
[18] M. Rameshkumar, P. Sivakumar, S. Sundaresh, K. Gopinath, Load sharing analysis of high-contact-ratio spur gears in military tracked vehicle applications, Gear Technol. 1 (2010) 43–50.
[19] M. Rameshkumar, G. Venkatesan, P. Sivakumar, Finite Element Analysis of High Contact Ratio Gear, AGMA Technical Paper (2010), 10FTM06.
[20] S.Y. Ye, S.J. Tsai, A computerized method for loaded tooth contact analysis of high-contact-ratio spur gears with or without flank modification considering tip corner contact and shaft misalignment, Mechanism and Machine, Theory 97 (2016) 190–214.
[21] V.I. Medvedev, A.E. Volkov, M.A. Volosova, O.E. Zubelevich, Mathematical model and algorithm for contact stress analysis of gears with multi-pair contact, Mech. Mach. Theory 86 (2015) 156–171.
[22] C. Gosselin, L. Cloutier, Q.D. Nguyen, A general formulation for the calculation of the load sharing and transmission error under load of spiral bevel and hypoid gears, Mech. Mach. Theory 30 (1995) 433–450.
[23] M. Kolivand, A. Kahraman, A load distribution model for hypoid gears using ease-off topography and shell theory, Mechanism and Machine Theory, 44 (2009) 1848–1865.
[24] S.H. Wu, S.J. Tsai, Contact stress analysis of concave conical gear drives, in: Proceedings of the First IFToMM Asian Conference Mechanism and Machine Science, October 22–25, Taipei, Taiwan, 2010.
[25] S.H. Wu, S.J. Tsai, Contact stress analysis of skew conical involute gear drives in approximate line contact, Mech. Mach. Theory 44 (2009) 1658–1676.
[26] R. Sun, C. Song, C. Zhu, Y. Wang, X. Yang, Computational studies on mesh stiffness of paralleled helical beveloid gear pair, Int. J. Precis. Eng. Manuf. 22 (2020) 123–137.
[27] R. Sun, C. Song, C. Zhu, X. Yang, X. Li, Computational study of pitting defect influence on mesh stiffness for straight beveloid gear, Eng. Fail Anal. (2021) 119.
[28] M. Stegemiller, D. Houser, A three-dimensional analysis of the base flexibility of gear teeth, (1993).

[29] S. Vaidyanathan, H. Busby, D. Houser, A numerical approach to the static analysis of an annular sector mindlin plate with applications to bevel gear design, Comput. Struct. 51 (1994) 255–266.
[30] E. Wellauer, A. Seireg, Bending strength of gear teeth by cantilever-plate theory, (1960).
[31] H.E. Merritt, Gears, Issac Pitman & Sons, 1951.
[32] B. Cao, G. Li, Computerized design of plunge shaving tool for beveloid gears and plunge shaving characteristic analysis, Mech. Mach. Theory (2021) 161.
[33] F.L. Litvin, A. Fuentes, Gear Geometry and Applied Theory, Cambridge University Press, 2004.
[34] I. Gonzalez-Perez, J.L. Iserte, A. Fuentes, Implementation of Hertz theory and validation of a finite element model for stress analysis of gear drives with localized bearing contact, Mech. Mach. Theory 46 (2011) 765–783.
[35] S. Li, Gear Contact model and loaded tooth contact analysis of a three-dimensional, thin-rimmed gear, J. Mech. Design 124 (2002) 511–517.
[36] Darrell, The finite element method, 2017.
[37] T.J.R. Hughes. The Finite Element Method: Linear Static and Dynamic Finite Element Analysis, Dover Publications, Mineola, NY, 2000.
[38] I. Amidror, Scattered data interpolation methods for electronic imaging systems: a survey, J. Electron. Imaging 11 (2002) 157–176.
[39] C. Liu, C. Tsay, Contact characteristics of beveloid gears, Mech. Mach. Theory 37 (2002) 333–350.
[40] S. Liu, C. Song, C. Zhu, G. Ni, N. Ullah, Concave and convex modifications analysis for skewed beveloid gears considering misalignments, Mech. Mach. Theory 133 (2019) 127–149.
[41] G. Ni, C. Zhu, C. Song, X. Du, Y. Zhou, Tooth contact analysis of crossed beveloid gear transmission with parabolic modification, Mech. Mach. Theory 113 (2017) 40–52.
[42] C. Zhu, L. Liu, C. Song, Y. Xiang, H. Liu, Pitch cone design and tooth contact analysis of intersected beveloid gears for marine transmission, Mechanism and Machine Theory, 82 (2014) 141–153.
[43] C. Zhu, C. Song, T.C. Lim, T. Peng, Pitch cone design and influence of misalignments on tooth contact behaviors of crossed beveloid gears, Mech. Mach. Theory 59 (2013) 48–64.
[44] Q. Liu, J.X. Wang, B.L. Yu, K. Xiao, Load distribution of straight beveloid gears with parallel axes, Adv. Mat. Res. 308-310 (2011) 1773–1777.